

PROPER MOTIONS AND STRUCTURAL PARAMETERS OF THE GALACTIC GLOBULAR CLUSTER M71

M. CADELANO^{1,2}, E. DALESSANDRO^{1,2}, F. R. FERRARO¹, P. MIOCCHI¹, B. LANZONI¹, C. PALLANCA¹ AND D. MASSARI^{2,3}

¹ Dipartimento di Fisica e Astronomia, Università di Bologna, Viale Berti Pichat 6/2, I-40127 Bologna, Italy

² INAF - Osservatorio Astronomico di Bologna, Via Ranzani 1, I-40127 Bologna, Italy and

³ Kapteyn Astronomical Institute, University of Groningen, P.O. Box 800, 9700 AV Gröningen, The Netherlands

(Dated: 18 november 2016)
 Draft version January 30, 2017

ABSTRACT

By exploiting two ACS/HST datasets separated by a temporal baseline of ~ 7 years, we have determined the relative stellar proper motions (providing membership) and the absolute proper motion of the Galactic globular cluster M71. The absolute proper motion has been used to reconstruct the cluster orbit within a Galactic, three-component, axisymmetric potential. M71 turns out to be in a low latitude disk-like orbit inside the Galactic disk, further supporting the scenario in which it lost a significant fraction of its initial mass. Since large differential reddening is known to affect this system, we took advantage of near-infrared, ground-based observations to re-determine the cluster center and density profile from direct star counts. The new structural parameters turn out to be significantly different from the ones quoted in the literature. In particular, M71 has a core and a half-mass radii almost 50% larger than previously thought. Finally we estimate that the initial mass of M71 was likely one order of magnitude larger than its current value, thus helping to solve the discrepancy with the observed number of X-ray sources.

Subject headings: Globular clusters: Individual: M71 (NGC 6838), proper motions, Techniques: photometric

1. INTRODUCTION

Galactic globular clusters (GCs) are dense and old ($t > 10$ Gyr) stellar systems containing up to $\sim 10^6$ stars, orbiting the Milky Way halo and bulge. Their study is crucial to understand the dynamical evolution of collisional systems (e.g. Meylan & Heggie 1997; Ferraro et al. 2012) and the interplay between dynamics and stellar evolution (e.g. Goodman & Hut 1989; Phinney 1993; Rasio et al. 2007; Ferraro et al. 2009, 2015). Their high central densities provide the ideal ground to the formation of exotic objects like blue straggler stars, cataclysmic variables, low-mass X-ray binaries and millisecond pulsars (e.g. Ferraro et al. 1997, 2003; Pooley et al. 2003; Ransom et al. 2005; Heinke et al. 2005).

In this respect, remarkable is the case of M71, which is a low-density GC located at a distance of about 4 kpc from Earth. It has a quite high metallicity ($[\text{Fe}/\text{H}] = -0.73$), a color excess $E(B - V) = 0.25$ (Harris 1996, 2010 edition) and a total mass of about $2 \times 10^4 M_\odot$ (Kimmig et al. 2015). X-ray observations revealed that it hosts a large population of X-ray sources, most likely consisting of stellar exotica. Surprisingly, as discussed in El-sner et al. (2008); Huang et al. (2010), the number of X-ray detections in M71 is significantly larger than what is expected from its present-day mass and its collisional parameter (which is a characteristic indicator of the frequency of dynamical interactions and thus of the number of stellar exotica in a GC; e.g. Bahramian et al. 2013). However, it is worth noticing that M71 is located at a low Galactic latitude ($l = 56.75^\circ$, $b = -4.56^\circ$), likely on a disk-like orbit (Geffert & Maintz 2000). Hence, it could have have lost a substantial fraction of its initial mass, due to heavy interactions with the Galactic field and to shocks caused by encounters with molecular clouds and/or spiral arms. Moreover the structural parameters

of this cluster have been estimated from shallow optical images (Peterson & Reed 1987), and therefore need to be re-determined more accurately. Hence, the value of the collisional parameter, which directly depends on the cluster structural parameters (Verbunt & Hut 1987), could be biased.

By taking advantage of two epoch of observations obtained with the *Hubble Space Telescope* (HST) and wide-field near-infrared and optical datasets for M71, here we present the determination of: (i) the stellar proper motions (which allow us to distinguish cluster members from Galactic contaminants), (ii) the absolute PM of the system (from which we estimate its orbit within the Galaxy during the last 3 Gyr), and (iii) the cluster gravitational center and structural parameters.

In Section 2 we describe the procedures adopted for the data reduction and analysis. Sections 3 and 4 are devoted to the determination of relative stellar proper motions (PMs), and of the cluster absolute PM and orbit, respectively. In Section 5 we present the new determination of cluster gravity center, density profile and structural parameters from near-infrared data and we study how the latter change if optical observations are used instead. We also provide an estimate of the initial mass of the system. Finally, in Section 6 we summarize the results and discuss the X-ray source abundance discrepancy in light of the new values of the cluster structural parameters and the initial mass estimate.

2. OBSERVATIONS AND DATA REDUCTION

The present work is based on two different datasets. Their characteristics and the adopted data reduction procedures are described in the following.

High-Resolution Dataset – This has been used to determine the stellar PMs. It consists of two sets of images acquired with the Wide Field Channel (WFC) of

the Advanced Camera for Surveys (ACS) mounted on HST (see Figure 1 for a map of the fields of view - FOVs - covered by these observations). This camera provides a FOV of $202'' \times 202''$ with a pixel scale of $0.05'' \text{ pixel}^{-1}$. The first epoch data have been collected under GO10775 (P.I.: Sarajedini) on 2006 July 1, and consist of a set of ten dithered images, five in the F606W filter (with exposure times: $1 \times 4 \text{ s}$; $4 \times 75 \text{ s}$) and five in the F814W filter ($1 \times 4 \text{ s}$; $4 \times 80 \text{ s}$). The second epoch is composed of proprietary data obtained under GO12932 (P.I.: Ferraro) on 2013, August 20. It consists of a set of ten deep images acquired through the F606W filter ($2 \times 459 \text{ s}$; $3 \times 466 \text{ s}$; $5 \times 500 \text{ s}$) and nine images in the F814W filter ($5 \times 337 \text{ s}$; $3 \times 357 \text{ s}$; $1 \times 440 \text{ s}$). The photometric analysis has been performed on the -file images (which are corrected for flat field, bias, dark counts and charge transfer efficiency) following the procedures described in detail in Anderson & King (2006). Briefly, both the epochs have been analyzed with the publicly available program `img2xym.WFC.09x10`, which uses a pre-determined model of a spatially varying point spread function (PSF) plus a single time-dependent perturbation PSF (to account for focus changes or spacecraft breathing). The final output of this process are two catalogs (one for each epoch) with instrumental magnitudes and positions for all the sources above a given threshold. Star positions were corrected in each catalog for geometric distortion by adopting the solution provided by Anderson & King (2006). By using the stars in common with the public catalog of Sarajedini et al. (2007, see also Anderson et al. 2008), instrumental magnitudes have been calibrated on the VEGAMAG system and instrumental positions have been reported on the absolute right ascension and declination coordinate reference system (α and δ , respectively). The final color-magnitude diagrams (CMDs) are shown in Figure 2 for the two different epochs.

Wide-field Dataset – To determine the cluster gravitational center and structural parameters, we used ground-based near-infrared images (Prop ID: 11AD90; PI: Thanjavur) obtained with the wide field imagers WIRCam mounted at the Canada-France-Hawaii Telescope (CFHT). To study the effect of differential reddening, we also made use of optical wide-field images (Prop ID: 04AC03, 03AC16; PI: Clem) acquired with MegaCam at the same telescope. The WIRCam camera consists of a mosaic of four chips of 2040×2040 pixels each, with a pixel scale of $0.31'' \text{ pixel}^{-1}$, providing a total FOV of $\sim 21.5' \times 21.5'$. We analyzed seven images obtained with the J and K_s filters, with exposure times of 5 s and 24 s, respectively. A dither pattern of few arcseconds was applied to fill the gaps among the detector chips. The MegaCam camera consists of a mosaic of 36 chips of 2048×4612 pixels each, with a pixel scale of $0.185'' \text{ pixel}^{-1}$ providing a FOV of $\sim 1^\circ \times 1^\circ$. A total of 50 images have been acquired, both in the g' and in the r' bands, with exposure times of 250 s each. A dither pattern of few arcseconds was adopted for each pointing, thus allowing the filling of most of the inter-chip gaps, with the exception of the most prominent, horizontal ones. Figure 3 shows the map of the Wide-field dataset.

For both these sets of observations, the images were pre-processed (i.e. bias and flat-field corrected) by means

of the Elixir pipeline developed by the CFHT team and the photometric analysis has been performed independently on each chip by following the procedures described in Dalessandro et al. (2015). Briefly, by means of an iterative procedure, an adequate number (> 20) of isolated and bright stars has been selected in each chip and filter to model the PSF. Hence, the PSF model has been applied to all the stellar-like sources at about 4σ from

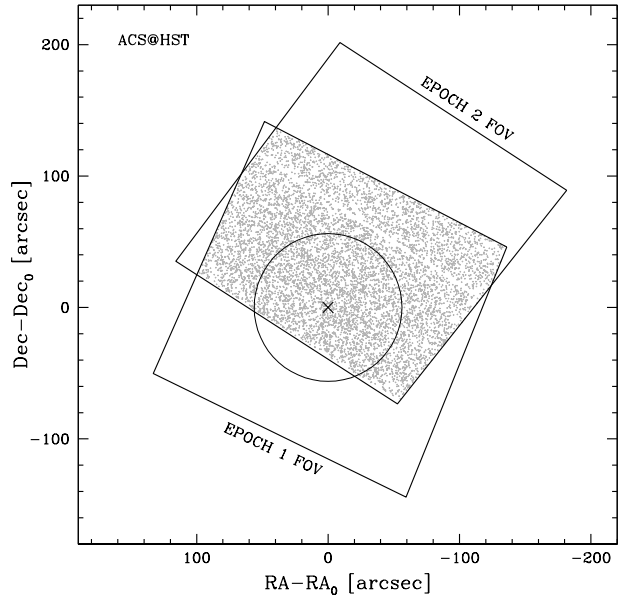


Figure 1. FOVs of the ACS first and second epoch datasets, centered on the newly estimated gravity center of M71 (black cross; see Section 5.1). The grey dots highlight the stars in common are between the two datasets, which has been used to measure the stellar proper motions. The solid circle marks the core radius of the cluster as derived in this work ($r_c = 56.2''$; see Section 5.2).

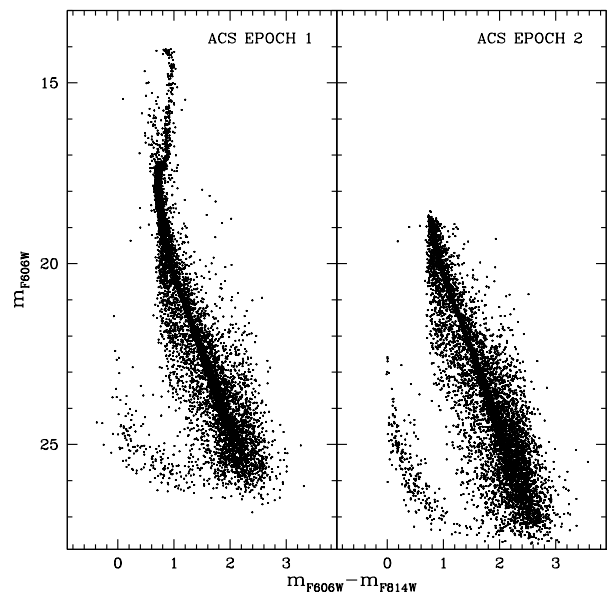


Figure 2. Optical CMD of M71 obtained from the first and second epoch ACS datasets (left and right panels, respectively).

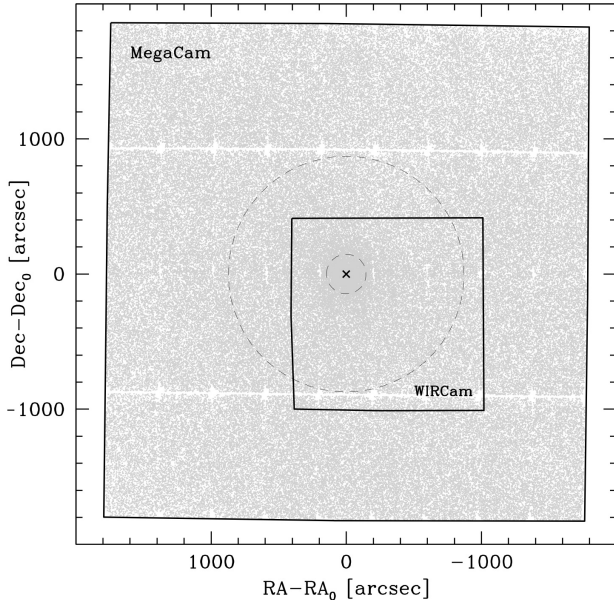


Figure 3. FOVs of the MegaCam and WIRCam datasets, centered on the cluster gravity center (black cross). The small and large dashed circles mark, respectively, the half-mass and the tidal radii derived in this work (see Section 5.2).

the local background by using DAOPHOT and the PSF-fitting algorithm ALLSTAR (Stetson 1987). For each filter and chip, we matched the single-frame catalogs to obtain a master list. Each master list includes the instrumental magnitudes, defined as the weighted mean of the single image measurements reported to the reference frame of the transformation, and the error, which is the standard deviation of the mean. Instrumental magnitudes have been reported to the SDSS photometric system¹ for the MegaCam catalog, and to the 2MASS system for the WIRCam catalog. Finally the instrumental positions have been reported to the absolute coordinate reference frame by using the stars in common with the 2MASS catalog². The CMDs for these datasets are shown in Figure 4 for stars located at less than 300'' from the center.

As can be seen from both Fig. 2 and Fig. 4, the standard evolutionary sequences are well defined. However, they are also heavily contaminated by foreground objects, as expected from the location of M71 close to the Galactic disk.

3. RELATIVE PROPER MOTIONS

To study the PMs of M71, we used the high resolution datasets. These are separated by a temporal baseline of 7.274 years and because of their different orientation, pointing and magnitude limit, the PM analysis could be performed only on the ~ 5000 stars in common, located in the overlapping FOV (see Figure 1) and having magnitudes $18 < m_{F814W} < 24$ (corresponding to magnitudes $19 < m_{F606W} < 25$). We adopted the procedure described in Massari et al. (2013, see also Dalessandro et al. 2013; Bellini et al. 2014; Massari et al. 2015).

¹ See <http://www.cfht.hawaii.edu/Science/CFHTLS-DATA/megaprimecalibration.html#P2>.

² Publicly available at <http://vizier.u-strasbg.fr>

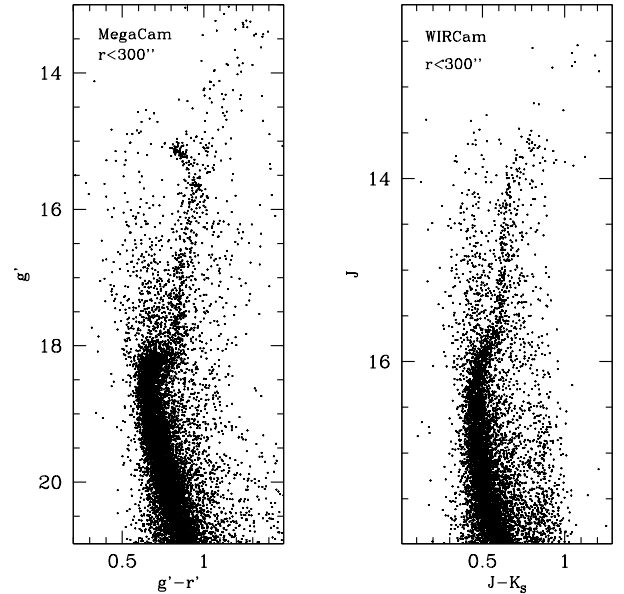


Figure 4. Optical and near-infrared CMDs of M71, obtained from the MegaCam (left panel) and the WIRCam datasets (right panel), respectively. In both cases, only stars within 300'' from the center are plotted.

Briefly, we used six parameters linear transformations³ to report the coordinates of the stars in each exposure to the distortion-free reference catalog of Sarajedini et al. (2007). Since we are interested in the stellar PMs relative to the cluster frame, these transformations have been determined by using a sample of ~ 6600 stars that, in the reference catalog, are likely cluster members on the basis of their CMD position (i.e. stars located along the main sequence). Moreover, the transformations have been determined independently on each detector chip in order to maximize the accuracy. At the end of the procedure, for each of the ~ 5000 stars we have up to ten position measurements in the first epoch catalog and up to nineteen in the second epoch catalog. To determine the relative PMs, we computed the mean X and Y positions of each star in each epoch, adopting a 3σ clipping algorithm. The star PMs are thus the difference between the mean X,Y positions evaluated in the two epochs, divided by $\Delta t = 7.274$ years. The resulting PMs are in units of pixels years⁻¹. Since the master frame is already oriented according to the equatorial coordinate system, the X-component of the PM corresponds to a projected PM along the (negative) RA and the Y-component corresponds to a PM along the Dec. Therefore, we converted our PMs in units of mas years⁻¹ by multiplying the previous values for the ACS pixel scale ($0.05''\text{pixel}^{-1}$), and we named $\mu_\alpha \cos(\delta)$ and μ_δ the PMs along the RA and Dec directions, respectively. To maximize the quality of our results, we built a final PM catalog by taking into account only stars for which at least three position measurements

³ To do this we applied six parameters linear transformations using CataXcorr, a code developed by P. Montegriffo at INAF-Osservatorio Astronomico di Bologna. This package is available at <http://dave2.bo.astro.it/?paolo/Main/CataPack.html>, and has been successfully used in a large number of papers by our group in the past 10 years.

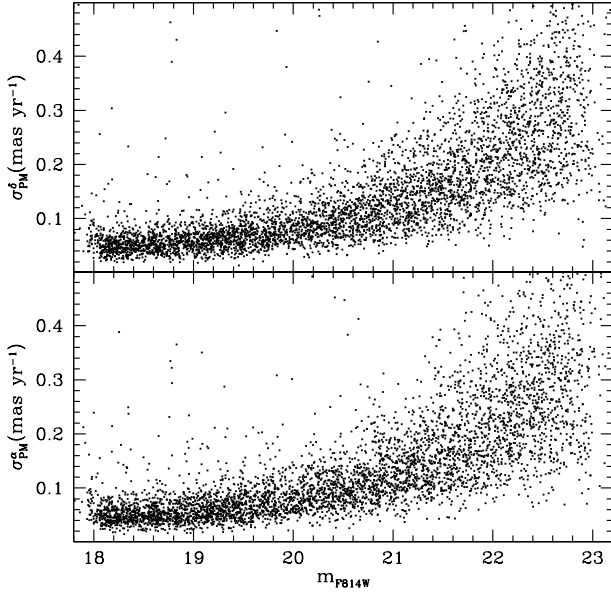


Figure 5. Estimated uncertainties of the derived proper motions as a function of the m_{F814W} magnitude of the measured stars. The upper and the lower panels show, respectively, the uncertainties in the RA and in the Dec directions. For stars with $m_{F814W} \lesssim 21$ the typical error is smaller than 0.07 mas yr^{-1} .

are available in each epoch. At the end of the procedure we counted 4938 stars with measured PMs. The errors in the position of the stars in each epoch ($\sigma_{1,2}^{\alpha,\delta}$) have been calculated as the standard deviation of the measured positions around the mean value. Then the errors in each component of the PM have been assumed as the sum in quadrature between the error in the first and second epoch: $\sigma_{PM}^{\alpha,\delta} = \sqrt{(\sigma_1^{\alpha,\delta})^2 + (\sigma_2^{\alpha,\delta})^2 / \Delta t}$. The errors as a function of the star magnitudes are shown in Figure 5. For both the PM directions, the typical uncertainty for stars with $m_{F814W} < 21$ is less of $\sim 0.07 \text{ mas yr}^{-1}$, demonstrating the good quality of our measurements. Following Bellini et al. (2014), we also verified that our PM measurements are not affected by chromatic effects, i.e., there is no dependence of $\mu_\alpha \cos(\delta)$ and μ_δ on the (F606W-F814W) color. Finally, our PM measurements are not even affected by positional effects, i.e., there is no dependence of the derived PMs on the instrumental (X,Y) positions.

In Figure 6 we show the PM distribution in the vector points diagram (VPD). As can be seen, the VPD is dominated by two prominent features: the clump in the center with zero relative PM is, by definition, dominated by the cluster population, while the elongated sparse distribution of points extending beyond this clump is dominated by contaminating field stars, mostly from the Galactic disk. At first inspection of the VPD we can see that only $\lesssim 60\%$ of the ~ 5000 analyzed stars are likely cluster members. A high percentage of field contamination is indeed expected in the case of M71, since it has a quite low stellar density and is located in a crowded field at low Galactic latitudes. By selecting in the VPD the likely cluster members (i.e. the stars with relative PM around 0 both in RA and in Dec) we find that the mean motion is 0.01 mas yr^{-1} with a standard deviation of 0.1 mas yr^{-1}

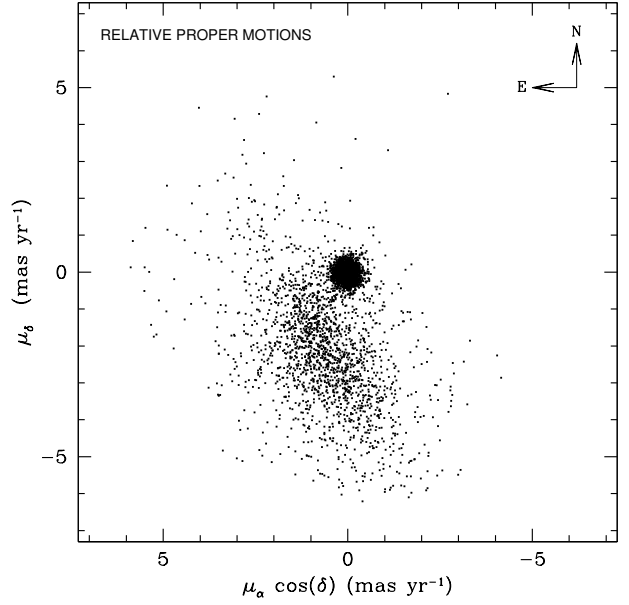


Figure 6. VPD of the relative PMs. The clump in the $(0,0) \text{ mas yr}^{-1}$ position is dominated by the cluster population. The elongated region beyond this clump is instead due to contaminating stars, mostly from the Galactic disk.

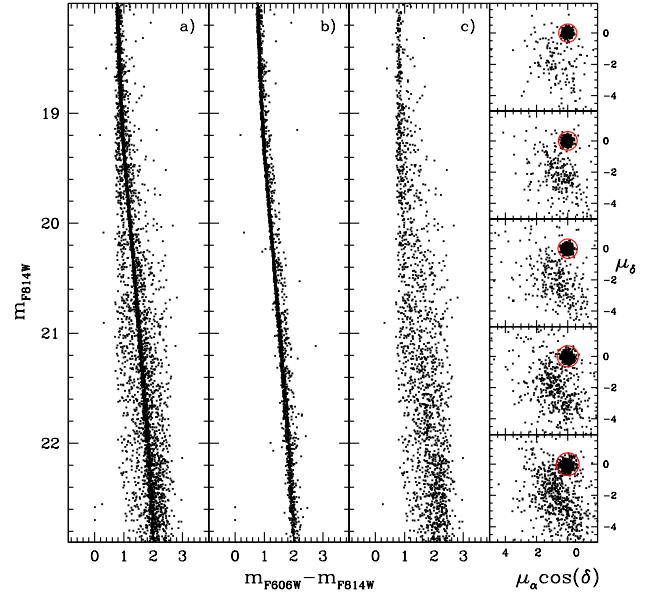


Figure 7. *Panel a:* Optical CMD of all the stars in common between the two observation epochs. *Panel b:* Decontaminated CMD obtained by using only the likely cluster members selected from the VPDs shown in the rightmost column. As can be seen, a sharper and more delineated main sequence and the binary sequence are now appreciable. *Panel c:* CMD made of all the contaminating objects, selected from the VPDs as those with PMs not compatible with the that of the GC. The Galactic sequence can be appreciate from this plot. *Rightmost column:* VPDs of the measured stars divided in bins of magnitudes. The solid red circles contain all the objects selected as likely cluster members.

both in α and in δ , thus, as expected, consistent with zero.

The effect of decontaminating the CMD from field stars

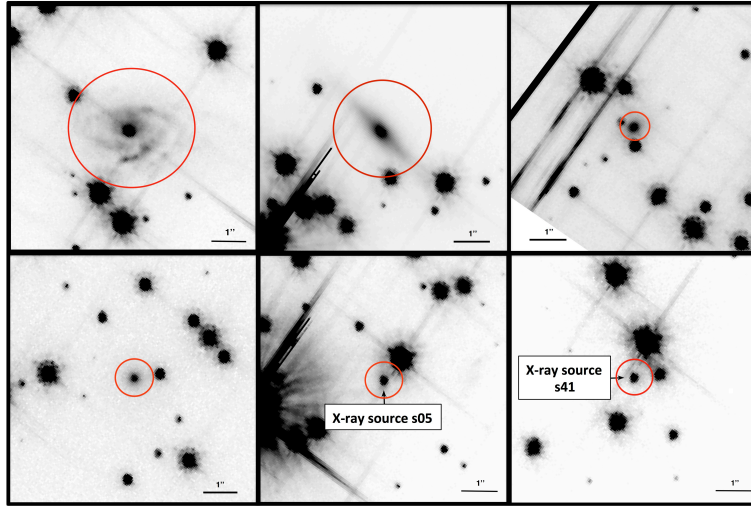


Figure 8. Finding charts of the six selected extra-Galactic objects used to determine the absolute reference frame zero point. The charts are taken from an ACS image acquired in the F814W filter. The three upper panels and the bottom-left panel show the four galaxies found through the visual inspection of the images. The central and right bottom panels show the optical counterparts to the X-ray sources s05 and s41, classified as AGNs. The point-like structure of these sources allowed a precise determination of the centroid position and of their PM.

is shown in Figure 7, where we have separated the objects with $PM \lesssim 0.6 \text{ mas yr}^{-1}$ (likely cluster members), from those with larger PMs. The selection of stars in the VPD is shown, per bins of one magnitude, in the left-hand column of the figure, with the objects having $PM \lesssim 0.6 \text{ mas yr}^{-1}$ encircled in red. The effect on the CMD is shown in the other three columns: from left to right, the observed CMD, the CMD of cluster members only, and the CMD of field stars. In the latter, it is well appreciable the main sequence of the Galactic field. Instead, the decontaminated CMD clearly shows a sharp and well defined main sequence, also revealing the binary sequence. The few stars on the blue side of the main sequence could be cluster exotic objects, such as cataclysmic variables, X-ray binaries or millisecond pulsars (e.g. Ferraro et al. 2001; Pallanca et al. 2010; Cohn et al. 2010; Cadelano et al. 2015), where a main sequence companion star is heated by a compact object. Nonetheless, we cannot completely rule out the possibility that some of these stars are field objects with PMs compatible with those of the cluster members.

4. ABSOLUTE PROPER MOTIONS

To transform the relative PMs into absolute ones, we used background galaxies as reference, since they have negligible PMs due to their large distances. This method has been successfully used in several previous works (e.g. Dinescu et al. 1999; Bellini et al. 2010; Massari et al. 2013). Unfortunately, the NASA Extragalactic Database report no sources in the FOV used for the PM estimate. Thus, we carefully inspected our images in order to search for diffuse galaxy-like objects. We found four galaxies with central point-like structure and relative high brightness, which allowed us to precisely determine their centroid position. Although many other galaxies are present in the FOV, they have no point-like struc-

ture or are too faint to allow the determination of a reasonable PM value. Moreover, as part of a project aimed at searching for optical counterparts to X-ray sources, we identified two promising active galactic nuclei (AGN) candidates. Two Chandra X-ray sources, named s05 and s41 in Elsner et al. (2008), have high energy and optical properties that can be attributed either to AGNs or to cataclysmic variables (see Huang et al. 2010, for more details). In order to distinguish between these two possibilities, we analyzed their PMs. We reported our relative PM reference frame to the absolute cluster PM ($\mu_\alpha \cos \delta, \mu_\delta = -3.0 \pm 1.4, -2.2 \pm 1.4 \text{ mas yr}^{-1}$) previously determined by Geffert & Maintz (2000) and found that these two sources have an absolute PM significantly different from the cluster motion and compatible with zero. We therefore conclude that these two objects are likely background AGNs⁴ and add them to the list of objects used to determine our reference absolute zero point. The six selected objects are located very close to each other in the VPD, as expected for extragalactic objects, and their finding charts are shown in Figure 8. We defined the absolute zero point as the weighted mean of their relative PMs and assumed as error the uncertainty on the calculated mean. By anchoring this mean position to the (0,0) mas yr^{-1} value, we find that the absolute PM of M71 is:

$$(\mu_\alpha \cos \delta, \mu_\delta) = (-2.7 \pm 0.5, -2.2 \pm 0.4) \text{ mas yr}^{-1}. \quad (1)$$

This value is in good agreement with (but more accurate than) the previous determination (Geffert & Maintz 2000), and it remains unchanged within the errors even if the two candidate AGNs are excluded from the analysis:

⁴ Of course, these sources could be foreground cataclysmic variables with PMs almost perfectly aligned with our line of sight, but this possibility seems to be quite unlikely.

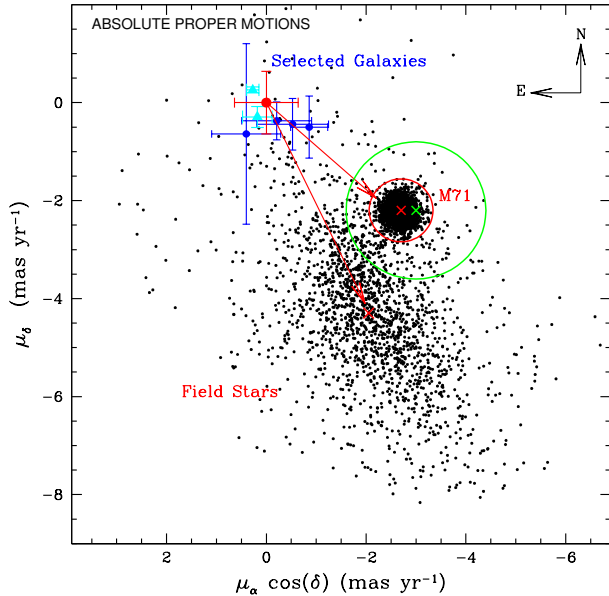


Figure 9. VPD of absolute PMs. The extra-Galactic objects used to determine the absolute reference frame zero point are marked as blue dots (galaxies) and cyan triangles (AGNs), and their mean motion is marked a large red dot. The red arrows indicate the absolute PM vectors of M71 and of the Galactic field population. The absolute PM value of M71 estimated in this work is marked with a red cross and the red circle represents its $\sim 1\sigma$ confidence region. The values previously determined in the literature (Geffert & Maintz 2000) are marked with a green cross and a green circle. The red cross centered on the elongated structure is centered on the field mean PM.

in that case we get: $(\mu_\alpha \cos \delta, \mu_\delta) = (-2.4 \pm 0.6, -1.9 \pm 0.1)$ mas yr $^{-1}$, still in agreement with the previous results. The VPD in the absolute frame is plotted in Figure 9, with the red and green crosses and circles marking, respectively, the absolute PM and its uncertainty as determined in this study and as quoted in Geffert & Maintz (2000).

Since every absolute PM measurement is strictly dependent on the accuracy of the absolute reference frame, we need to verify the possible presence of systematic errors in its determination. One of the possible source of systematic errors is the rotation of the GC on the plane of the sky. Indeed, since we used only cluster stars to define the relative reference frame, if the GC is rotating, then our frame will be rotating too. This would introduce an artificial rotation to background and foreground objects around the cluster center. To quantify this possible effect we followed the procedure described in Massari et al. (2013). We selected a sample of field stars as those that in the VPD of Figure 6 have relative PMs larger than 0.8 mas yr $^{-1}$. Then we decomposed their PM vectors into a radial and tangential component with respect to the cluster center. If the GC is rotating, we would expect to find a clear dependence of the PM tangential component on the distance from the cluster center. Such a dependence is however excluded by our results, thus that the internal regions of M71 are not rotating, in agreement with the recent findings by Kimmig et al. (2015).

We also compared the field star motion to that expected from theoretical Galactic models in the analyzed

FOV. To evaluate the field mean motion, we followed the procedure described in Anderson & van der Marel (2010). First, we excluded the stars within 0.8 mas yr $^{-1}$ from the cluster mean motion. Then we iteratively removed field stars in a symmetric position with respect to the GC exclusion region and evaluated the weighted mean motion by applying a 3σ algorithm. We found $(\mu_\alpha \cos \delta, \mu_\delta) = (-2.0 \pm 0.2, -4.3 \pm 0.2)$ mas yr $^{-1}$. We compared these values with those predicted for the same region of the sky in the Besançon Galactic model (Robin et al. 2003), simulating a sample of ~ 2000 artificial stars distant up to 15 kpc from the Galactic center, in a FOV centered on M71, covering a solid angle of $\sim 11'$, and having V magnitudes ranging 12 from to 25. The predicted field mean motion is $(\mu_\alpha \cos \delta, \mu_\delta) = (-2.4, -4.7)$ mas yr $^{-1}$, in good agreement with our results.

4.1. The cluster orbit

The GC absolute PM, combined with the radial velocity $v_r = -23.1 \pm 0.3$ km s $^{-1}$ from Kimmig et al. (2015), can be used to determine 3D space velocity of the cluster in a Cartesian Galactocentric rest frame. Using the formalism described in Johnson & Soderblom (1987), assuming the Local Standard of Rest velocity equal to 256 km s $^{-1}$ (Reid et al. 2009) and using the value of the Sun velocity with respect to it from Schönrich et al. (2010), we obtained $(v_x, v_y, v_z) = (52 \pm 10, 204 \pm 6, 31 \pm 12)$ km s $^{-1}$, where the major source of uncertainty is the GC absolute PM error. We then used the 3D velocity of the cluster and its current Galactocentric position⁵ $(x, y, z) = (-6.2 \pm 0.6, 3.4 \pm 0.3, -0.32 \pm 0.03)$ kpc, to reconstruct its orbit in the axisymmetric potential discussed in Allen & Santillan (1991), which has been extensively used to study the kinematics of Galactic stellar systems (e.g. Ortolani et al. 2011; Moreno et al. 2014; Massari et al. 2015). The orbit was time-integrated backwards, starting from the current conditions and using a second-order leapfrog integrator (e.g. Hockney & Eastwood 1988) with a small time step of ~ 100 kyr. Since the adopted Galactic potential is static, we choose to back-integrate the orbit only for 3 Gyr, since longer backward integrations become uncertain due to their dependence on the Galactic potential variations as a function of time. This numerical integration required about 32000 steps and reproduced ~ 20 complete cluster orbits. The errors on the conservation of the energy and the Z-component of the angular momentum never exceeded one part over 10^9 and 10^{16} , respectively. We generated a set of 1000 clusters starting from the phase-space initial conditions normally distributed within the uncertainties. For all of these clusters we repeated the backward time integration. Figure 10 shows the resulting cluster orbits in the equatorial and meridional Galactocentric plane. As can be seen, the cluster has a low-latitude disk-like orbit within the Galactic disk. Indeed in the equatorial plane it reaches a maximum distance of ~ 8 kpc from the Galactic center and a minimum distance of ~ 5 kpc. Thus, it orbits around the assumed spheroidal bulge, never crossing it.

⁵ We adopted the Galactic coordinates quoted in Harris (1996) and the convention in which the X axis points opposite to the Sun, i.e., the Sun position is $(-8.4, 0, 0)$, where the distance of the Sun from the Galactic center is from Reid et al. (2009).

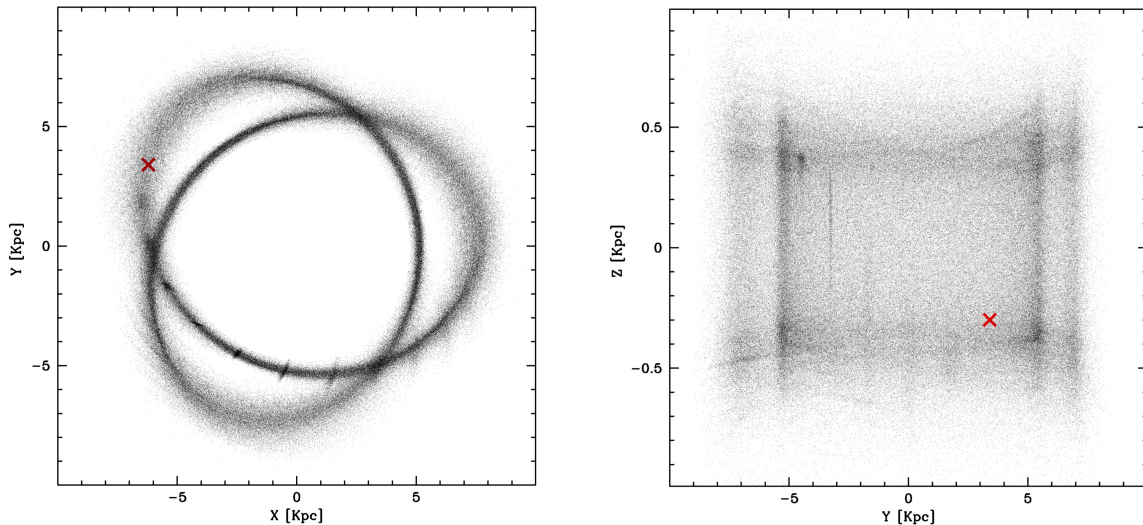


Figure 10. *Left:* Simulated positions occupied by M71 during the last 3 Gyr along its orbit in the equatorial Galactic plane. Each point represents the position of one (out of 1000) cluster in one of the 32000 snapshots obtained during the numerical integration. The red cross marks the current cluster position. *Right:* Same as in the left panel, but for the orbit in the meridional Galactic plane.

Moreover, it persists on a low-latitude orbit, with a typical height from the Galactic plane of about ± 0.4 kpc, thus again confined within the disk. The estimated orbits indicate that, at least during the last 3 Gyr, M71 tightly interacted with the inner Galactic disk. With respect to the large majority of Galactic GCs, which are on large orbits across the (low-density) halo, these interactions likely induced heavy mass-loss (Vesperini & Heggie 1997) in M71, thus supporting the possibility that it lost a significant fraction of its initial mass, as already suggested by its flat mass function (De Marchi et al. 2007). Moreover, such a heavy mass-loss could finally explain why M71 harbors a large population of X-ray sources, in spite of its present low mass (Elsner et al. 2008).

5. GRAVITATIONAL CENTER, STRUCTURAL PARAMETERS AND INITIAL MASS

In this section we present the determination of the gravitational center and of the new structural parameters of M71.

5.1. Gravitational center

To avoid biases due to the strong differential reddening affecting the system (e.g. Schlegel et al. 1998), for the determination of the cluster center of gravity C_{grav} we used the near-infrared WIRCam catalog, which has the same level of completeness of the ACS one in the magnitude range $14 < K_s < 16.8$. C_{grav} has been determined following an iterative procedure that, starting from a first-guess center, selects a sample of stars within a circle of radius r and re-determine the center as the average of the star coordinates (α and δ). The procedure stops when convergence is reached, i.e., when the newly-determined center coincides with the previous ones within an adopted tolerance limit (Lanzoni et al. 2010, see also Montegriffo et al. 1995; Lanzoni et al. 2007). For M71, which is a relative loose GC (Harris 1996), we repeated the procedure eighteen times, using different values of r and selecting stars in different magnitude ranges, chosen as a compromise between having high enough statistics and avoiding spurious effects due to incompleteness and saturation. In particular, the radius r has been chosen in

the range $140'' - 160''$ with a step of $10''$, thus guaranteeing that it is always larger than the literature core radius $r_c = 37.8''$ (Harris 1996). For each radius r , we have explored six magnitude ranges, from $K_s > 14$ (in order to exclude stars close to the saturation limit), down to $K_s = 16.3 - 16.8$, in steps of 0.1 magnitudes. As first-guess center we used that quoted by Goldsbury et al. (2010). The final value adopted as C_{grav} is the mean of the different values of RA and Dec obtained in the eighteen explorations, and its uncertainty is their standard deviation. We found $\text{RA} = 19^{\text{h}}53^{\text{m}}46.106^{\text{s}}$ and $\text{Dec} = +18^{\circ}46'43.38''$, with an uncertainty of about $1.7''$. The newly determined center of M71 is $\sim 5.7''$ west and $\sim 0.3''$ north from the one measured from optical ACS data by Goldsbury et al. (2010). Such a discrepancy is likely ascribable to an effect of differential reddening impacting the optical determination.

5.2. Stellar density profile

Since the surface brightness profile can suffer from strong biases and fluctuations due to the presence of few bright stars (see, e.g., the case of M2 in Dalessandro et al. 2009), in order to re-evaluate the structural parameters of M71 we used direct star counts. The determination of the stellar density profile (number of stars per unit area, in a series of concentric annuli around C_{grav}) has been performed following the procedure fully described in Miocchi et al. (2013). Also in this case, in order to minimize the differential reddening effect we used the near-infrared WIRCam data, which covers distances out to $\sim 1000''$ from C_{grav} in the south-west portion of the cluster (see Fig. 3). To build the density profile we considered 13 concentric annuli around C_{grav} , each one divided into four sub-sectors. We then counted the number of stars with $14 < K_s < 16.5$ in each sub-sector and divided it by the sub-sector area. The projected stellar density in each annulus is the mean of the values measured in each sub-sector and the uncertainty has been estimated from the variance among the sub-sectors. The stellar background has been estimated by averaging the outermost values, where the profile flattens, and it has

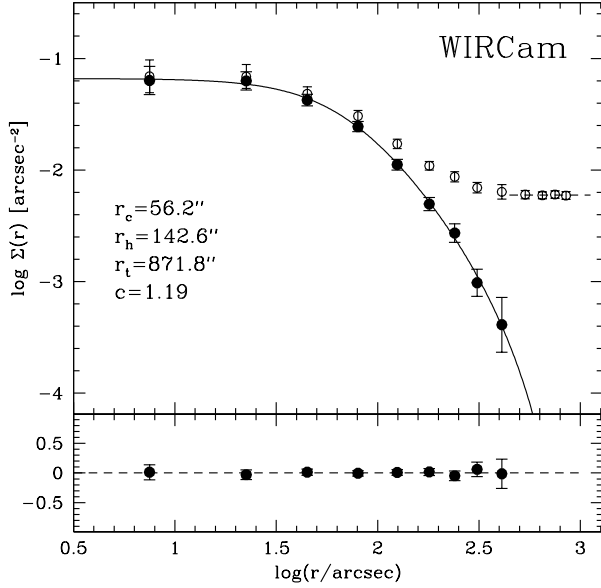


Figure 11. Observed density profile of M71 obtained from the WIRCam near-infrared dataset (open circles). The dashed line marks the density value of the Galactic field background, obtained by averaging the four outermost points. The black filled circles are the density values obtained after background subtraction (see Section 5.2). The best-fit King model (solid line) is overplotted to the observations and the residuals of the fit are reported in the bottom panel. The best-fit structural parameters are also labelled in the figure.

been subtracted to the observed distribution to obtain decontaminated density profiles. The result is shown in Figure 11.

The cluster structural parameters has been derived by fitting the observed density profiles with a spherical, isotropic, single-mass King (1966) model.⁶ The single-mass approximation is justified by the fact that the magnitude range chosen to build the profile includes cluster stars with negligible mass differences. The best-fit model results in a cluster with a King dimensionless potential $W_0 = 5.55 \pm 0.35$, a core radius $r_c = 56.2^{+4.5}_{-4.0}$ arcsec, a half-mass radius $r_h = 146.2^{+11.5}_{-10.0}$ arcsec, a truncation radius $r_t = 871.8^{+247}_{-164}$ arcsec and, thus, a concentration parameter, defined as the logarithm of the truncation to the core radius, $c = \log r_t/r_c = 1.19$.

There is a significant difference between these parameters and those quoted in the Harris (1996) catalog, originally estimated by Peterson & Reed (1987) from a surface brightness profile obtained from shallow optical images: $r_c = 37.8''$, $r_h = 100.2''$ and $r_t = 533.9''$ (the latter being derived from the quoted value of the concentration parameter: $c = 1.15$). To further investigate this discrepancy, we built the cluster surface brightness profile using a K-band 2MASS image, and we found that it is in agreement with the number density profile shown in Figure 11, thus further reinforcing the reliability of the newly-determined parameters. On the other hand, if we take into account only the brightest pixels of the K-band

image, we find a surface brightness profile consistent with the literature one. This implies that the structural parameters quoted in the literature (which are determined from the light of the most luminous giants only) are not representative of the overall cluster profile.

The availability of a very wide ($\sim 1^\circ \times 1^\circ$) sample at optical wavelengths (the MegaCam dataset) with an analogous level of completeness (comparable to the ACS one for $13 < g' < 19$) allowed us to investigate how the derivation of the cluster stellar number density profile from optical observations can be affected by the presence of large differential extinction. Figure 12 compares the extinction map and the 2D density map of the $1500'' \times 1500''$ region of the sky centered on M71. The former is obtained from Schlegel et al. (1998) and shows that the color excess $E(B - V)$ varies from ~ 0.24 to ~ 0.54 , with several “spots” and a clear gradient across the field. The density map in the right-hand panel shows the number of stars with $13 < g' < 19$, per unit area, detected in the MegaCam sample. As expected, at large scales it reveals a direct correspondence with the extinction map: in particular, the stellar density manifestly drops in the north-west sector, where the color excess is the highest, while the opposite is true in the south-east part of the cluster. Obviously, this is expected to significantly impact the density profile obtained from star counts in the optical bands.

To quantitatively test this effect, we determined the cluster density profile by using the MegaCam (optical) data. The result is plotted in Figure 13 and shows that, indeed, the structural parameters of the best-fit King model turn out to be very different from those obtained from the near-infrared (almost reddening-unaffected) dataset (compare with Fig. 11). In particular, the concentration parameter is much larger ($c = 1.6$), as a consequence of a comparable core radius ($r_c = 58''$ versus $56.2''$), but a more than doubled truncation radius ($r_t = 2347.8''$ versus $871.8''$). Such a severe over-estimate of r_t is due to the high extinction affecting the external portions of the MegaCam sample, where the Galactic field background is evaluated, and it clearly demonstrates how important is to take differential reddening under control for the determination of a cluster density profile.

5.3. Cluster initial mass

In Sect. 4.1 we have argued that M71 likely lost a significant fraction of its original mass, mostly due to environmental effects. In this section, we attempt to estimate the total cluster initial mass. Although many recipes can be used to this aim (e.g. Vesperini et al. 2013), we adopted the simple analytical approach described in Lamers et al. (2005); Lamers & Gieles (2006). It describes the way a cluster loses its mass due to the effects of both stellar and dynamical evolution (including processes such as interactions with the Galactic tidal field and shocks due to encounters with giant molecular clouds or spiral arms). Although this method has been developed specifically for open clusters, it can be used also in the case of M71, since its current mass ($M = 2.0^{+1.6}_{-0.9} \times 10^4 M_\odot$; from Kimmig et al. 2015) and orbit are consistent with those typical of open clusters (see also Dalessandro et al. 2015, for a similar implementation of this procedure). The initial mass M_{ini} of the

⁶ These models can be generated and freely downloaded from the Cosmic-Lab web site: <http://www.cosmic-lab.eu/Cosmic-Lab/Products.html>. The fitting procedure is fully described in Micocchi et al. (2013)

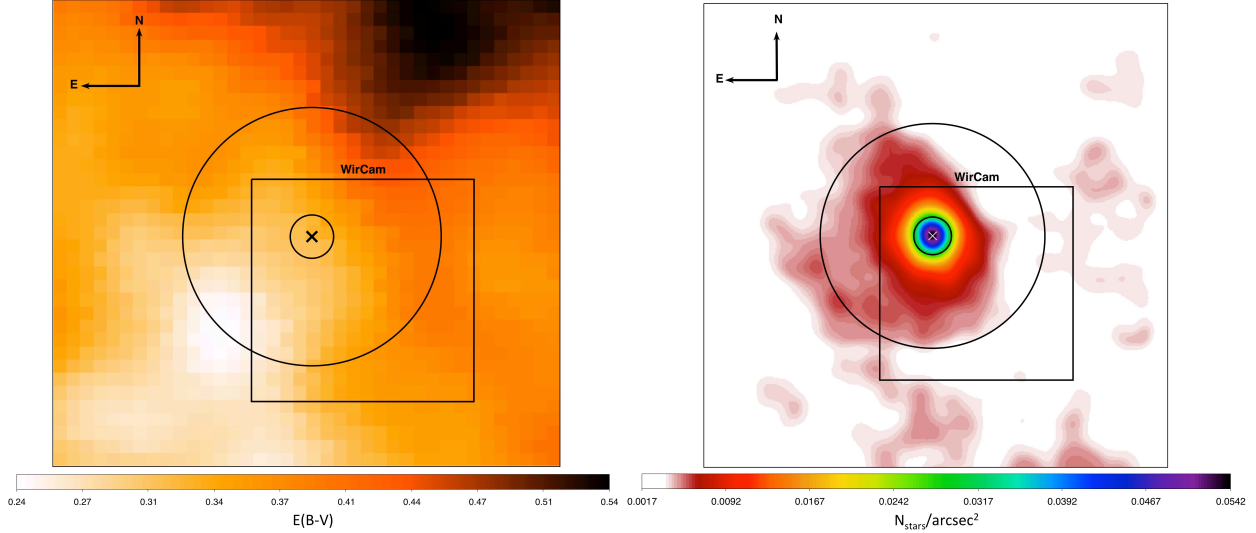


Figure 12. *Left Panel:* Reddening map (from Schlegel et al. 1998) of the $1500'' \times 1500''$ region centered on M71. The small and large circles mark, respectively, the half-mass and truncation radii of the cluster. The square marks the FOV of the WIRCam dataset. The presence of severe differential reddening across the system, especially in the north-west sector, is apparent. *Right Panel:* 2D stellar density map in the same region of the left panel, obtained by counting all the stars with $13 < g' < 19$ in the optical (MegaCam) dataset. The comparison with the reddening map on the left makes the effect of extinction well visible: the significant decline in the stellar density observed in the external regions of the map (especially in the north-east sector) is clearly due to the presence of thick dust clouds.

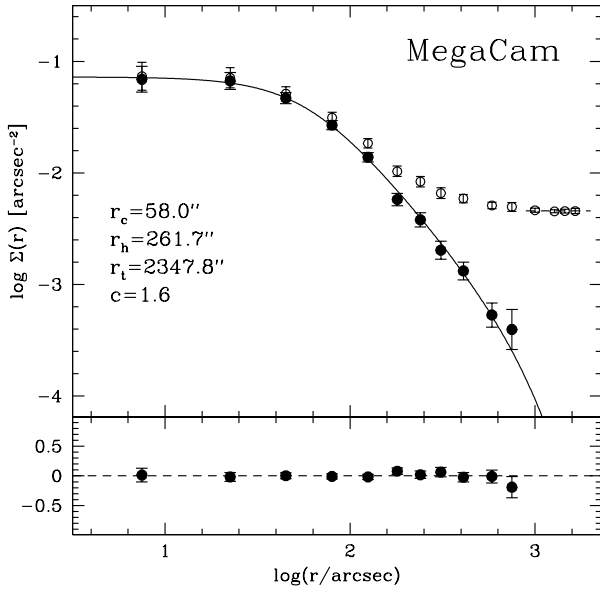


Figure 13. Density profile of M71 obtained from the optical (MegaCam) dataset. The meaning of all symbols and lines is as in Fig. 11. The best-fit King model parameters (especially the truncation radius and the concentration) are significantly different from those obtained from near-infrared observations, mainly because the Galactic background is underestimated at optical wavelengths, due to the large differential reddening affecting the external regions of the covered FOV (compare to Fig. 12).

cluster can be expressed as follows:

$$M_{\text{ini}} \simeq \left[\left(\frac{M}{M_{\odot}} \right)^{\gamma} + \frac{\gamma t}{t_0} \right]^{\frac{1}{\gamma}} [1 - q_{\text{ev}}(t)]^{-1}, \quad (2)$$

where M is the cluster current mass, $t = 12 \pm 1$ Gyr is the cluster age (Di Cecco et al. 2015), t_0 is the dissolution time-scale parameter, γ is a dimensionless index

and $q_{\text{ev}}(t)$ is a function describing the mass-loss due to stellar evolution. The dissolution time-scale parameter is a constant describing the mass-loss process, which depends on the strength of the tidal field. Small values of t_0 are typically associated with encounters with molecular clouds and spiral arms, while larger values are used to describe the effect of the Galactic tidal field (see Lamers et al. 2005). Since M71 has an orbit and a structure quite similar to those of open clusters, we assumed t_0 in the same range of values ($2.3 < t_0 < 4.7$ Myr) constrained in Lamers et al. (2005). The parameter γ depends on the cluster initial density distribution and is usually constrained by the value of the King dimensionless potential W_0 . We adopted $\gamma = 0.62$, corresponding to $W_0 = 5$, a typical value for an averagely concentrated cluster. The function $q_{\text{ev}}(t)$, which describes the mass-loss process due to stellar evolution, can be approximated by the following analytical expression:

$$\log q_{\text{ev}}(t) = (\log t - a)^b + c, \quad \text{for } t > 12.5 \text{ Myr}, \quad (3)$$

where a , b and c are coefficients that depend on the cluster metallicity. The iron abundance ratio of M71 is $[\text{Fe}/\text{H}] = -0.73$ (Harris 1996), which corresponds to $a = 7.03$, $b = 0.26$ and $c = -1.80$ (Lamers et al. 2005).

The resulting initial mass of the cluster is shown in Figure 14 as a function of the explored range of values of t_0 . It varies between 1.8 and $6.8 \times 10^5 M_{\odot}$, which are all values typical of the mass of Galactic halo GCs, and is one order of magnitude (or more) larger than the current mass. Also considering the largest possible value of t_0 (~ 30 Myr; see Lamers et al. 2005), we find that the cluster initial mass is at least twice its current value. Clearly, this estimate is based on a simplified approach and on parameters derived by the average behaviors of open clusters, and different assumptions may lead to different results. However, it is interesting to note that, while such a high mass loss would be unlikely for a halo GC, it can be reasonable for a system moving along an

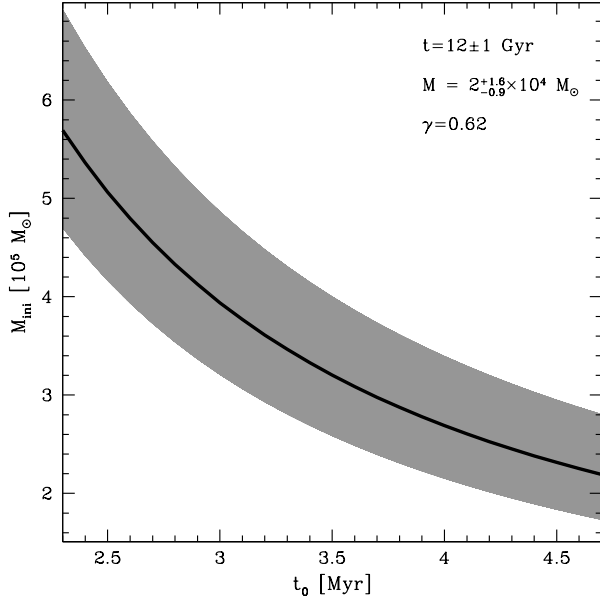


Figure 14. Initial mass of M71 as a function of the dissolution time-scale parameter t_0 , estimated as described in Sect. 5.3. The black curve shows the values obtained by assuming a cluster current mass of $2 \times 10^4 M_\odot$ and an age of 12 Gyr. The gray shaded area includes all the values determined by considering the uncertainties in these quantities (see labels).

orbit confined within the disk (see Sect. 4.1).

6. SUMMARY AND CONCLUSIONS

By using two high-resolution ACS datasets separated by a temporal baseline of ~ 7 years, we determined the relative PMs of ~ 5000 individual stars in the direction of the low-mass GC M71, finding that only $\sim 60\%$ of them have PMs consistent with being members of the cluster. The identification of four galaxies and two AGNs within the sampled FOV, allowed us to also constrain the absolute PM of M71. This has been used to infer the orbit of the cluster within the Galactic potential well, which has been modeled by using a three-component axisymmetric analytic model. It turned out that, at least during the last 3 Gyr, M71 has been in a disk-like orbit confined within the Galactic disk. It therefore seems reasonable to suppose that M71 suffered a number of dynamical processes (e.g., with the dense surrounding environment, the Milky Way spiral arms, various molecular clouds) that made it lose an amount of mass significantly larger than what expected for the majority of Galactic GCs, which are on halo-like orbits. We re-determined the gravitational center and density profile of M71 by using resolved star counts from a wide-field near-infrared catalog obtained with WIRCam at the CFHT. This allowed us to minimize the impact of the large and differential reddening affecting the system. With respect to the values quoted in the literature (which have been determined from optical data), we found the cluster centre to be located almost $6''$ to the west, a $\sim 50\%$ larger core and half-mass radii. Finally, we used a simplified analytical approach to take into account mass-loss processes due to stellar and dynamical evolution, and thus estimate the initial cluster mass, finding that the system likely was one order of magnitude more massive than its current

value.

As discussed in Sect. 1, M71 is known to harbor a rich population of X-ray sources (Elsner et al. 2008), in a number that exceeds the predictions based on the values of its mass and its collision parameter Γ (Huang et al. 2010). Since this latter depends on the cluster central luminosity density and core radius ($\Gamma \propto \rho_0^{1.5} r_c^2$; Verbunt & Hut 1987; Huang et al. 2010), we have re-evaluated it by using the newly determined structural parameters. By adopting the central surface brightness quoted in Harris (1996) and equation (4) in Djorgovski (1993), we found $\log \rho_0 = 2.60$ (in units of L_\odot/pc^{-3}). From this quantity and the value of r_c here determined, the resulting value of Γ is about half the one quoted in Huang et al. (2010), and the discrepancy in terms of the expected number of X-ray sources aggravates. Instead, the much larger initial mass here estimated for the system would be able to naturally account for the currently observed X-ray population, thus reinforcing the hypothesis that M71 lost a large fraction of stars during its orbit. An accurate investigation of the possible presence of tidal tails around the cluster would be important to confirm such a significant mass-loss from the system. However, this is currently hampered by the large differential reddening affecting this region of the sky, and a wide-field infrared observations are urged to shed light on this issue.

7. ACKNOWLEDGEMENT

We warmly thank the referee, whose useful comments improved the quality of the manuscripts.

REFERENCES

- Allen, C., & Santillan, A. 1991, *Rev. Mexicana Astron. Astrofis.*, 22, 255
- Anderson, J., & King, I. R. 2006, *Instrument Science Report ACS* 2006-01, 34 pages, 1
- Anderson, J., Sarajedini, A., Bedin, L. R., et al. 2008, *AJ*, 135, 2055
- Anderson, J., & van der Marel, R. P. 2010, *ApJ*, 710, 1032
- Bahramian, A., Heinke, C. O., Sivakoff, G. R., & Gladstone, J. C. 2013, *ApJ*, 766, 136
- Bellini, A., Piotto, G., Bedin, L. R., et al. 2009, *A&A*, 493, 959
- Bellini, A., Bedin, L. R., Pichardo, B., et al. 2010, *A&A*, 513, A451
- Bellini, A., Anderson, J., van der Marel, R. P., et al. 2014, *ApJ*, 797, 115
- Cadelano, M., Pallanca, C., Ferraro, F. R., et al. 2015, *ApJ*, 807, 91
- Cohn, H. N., Lugger, P. M., Couch, S. M., et al. 2010, *ApJ*, 722, 20
- Cudworth, K. M. 1985, *AJ*, 90, 65
- Cudworth, K. M., & Hanson, R. B. 1993, *AJ*, 105, 168
- Dalessandro, E., Beccari, G., Lanzoni, B., et al. 2009, *ApJS*, 182, 509
- Dalessandro, E., Ferraro, F. R., Massari, D., et al. 2013, *ApJ*, 778, 135
- Dalessandro, E., Miocchi, P., Carraro, G., Jílková, L., & Moitinho, A. 2015, *MNRAS*, 449, 1811
- Djorgovski, S. 1993, *Structure and Dynamics of Globular Clusters*, 50, 373
- De Marchi, G., Paresce, F., & Pulone, L. 2007, *ApJ*, 656, L65
- Di Cecco, A., Bono, G., Prada Moroni, P. G., et al. 2015, *AJ*, 150, 51
- Dinescu, D. I., van Altena, W. F., Girard, T. M., & López, C. E. 1999, *AJ*, 117, 277
- Elsner, R. F., Heinke, C. O., Cohn, H. N., et al. 2008, *ApJ*, 687, 1019
- Ferraro, F. R., Paltrinieri, B., Fusi Pecci, F., et al. 1997, *A&A*, 324, 915
- Ferraro, F. R., D'Amico, N., Possenti, A., Mignani, R. P., & Paltrinieri, B. 2001, *ApJ*, 561, 337
- Ferraro, F. R., Sills, A., Rood, R. T., Paltrinieri, B., & Buonanno, R. 2003, *ApJ*, 588, 464

- Ferraro, F. R., Beccari, G., Dalessandro, E., et al. 2009, *Nature*, 462, 1028
- Ferraro, F. R., Lanzoni, B., Dalessandro, E., et al. 2012, *Nature*, 492, 393
- Ferraro, F. R., Lanzoni, B., Dalessandro, E., Mucciarelli, A., & Lovisi, L. 2015, *Ecology of Blue Straggler Stars*, 99
- Geffert, M., & Maintz, G. 2000, *A&AS*, 144, 227
- Goldsbury, R., Richer, H. B., Anderson, J., et al. 2010, *AJ*, 140, 1830
- Goodman, J., & Hut, P. 1989, *Nature*, 339, 40
- Harris, W. E. 1996, *AJ*, 112, 1487
- Heinke, C. O., Grindlay, J. E., Edmonds, P. D., et al. 2005, *ApJ*, 625, 796
- Hockney, R. W., & Eastwood, J. W. 1988, *Bristol: Hilger*, 1988,
- Huang, R. H. H., Becker, W., Edmonds, P. D., et al. 2010, *A&A*, 513, A16
- Kimmig, B., Seth, A., Ivans, I. I., et al. 2015, *AJ*, 149, 53
- King, I. R. 1966, *AJ*, 71, 64
- Johnson, D. R. H., & Soderblom, D. R. 1987, *AJ*, 93, 864
- Lamers, H. J. G. L. M., Gieles, M., Bastian, N., et al. 2005, *A&A*, 441, 117
- Lamers, H. J. G. L. M., & Gieles, M. 2006, *A&A*, 455, L17
- Lanzoni, B., Dalessandro, E., Ferraro, F. R., et al. 2007, *ApJ*, 668, L139
- Lanzoni, B., Ferraro, F. R., Dalessandro, E., et al. 2010, *ApJ*, 717, 653
- Massari, D., Bellini, A., Ferraro, F. R., et al. 2013, *ApJ*, 779, 81
- Massari, D., Dalessandro, E., Ferraro, F. R., et al. 2015, *ApJ*, 810, 69
- Meylan, G., & Heggie, D. C. 1997, *A&A Rev.*, 8, 1
- Miocchi, P., Lanzoni, B., Ferraro, F. R., et al. 2013, *ApJ*, 774, 151
- Montegriffo, P., Ferraro, F. R., Fusi Pecci, F., & Origlia, L. 1995, *MNRAS*, 276, 739
- Moreno, E., Pichardo, B., & Velázquez, H. 2014, *ApJ*, 793, 110
- Ortolani, S., Barbuy, B., Momany, Y., et al. 2011, *ApJ*, 737, 31
- Pallanca, C., Dalessandro, E., Ferraro, F. R., et al. 2010, *ApJ*, 725, 1165
- Peterson, C. J., & Reed, B. C. 1987, *PASP*, 99, 20
- Phinney, E. S. 1993, *Structure and Dynamics of Globular Clusters*, 50, 141
- Pooley, D., Lewin, W. H. G., Anderson, S. F., et al. 2003, *ApJ*, 591, L131
- Ransom, S. M., Hessels, J. W. T., Stairs, I. H., et al. 2005, *Science*, 307, 892
- Rasio, F. A., Baumgardt, H., Corongiu, A., et al. 2007, *Highlights of Astronomy*, 14, 215
- Reid, M. J., Menten, K. M., Zheng, X. W., et al. 2009, *ApJ*, 700, 137-148
- Robin, A. C., Reylé, C., Derrière, S., & Picaud, S. 2003, *A&A*, 409, 523
- Sarajedini, A., Bedin, L. R., Chaboyer, B., et al. 2007, *AJ*, 133, 1658
- Schlegel, D. J., Finkbeiner, D. P., & Davis, M. 1998, *ApJ*, 500, 525
- Schönrich, R., Binney, J., & Dehnen, W. 2010, *MNRAS*, 403, 1829
- Stetson, P. B. 1987, *PASP*, 99, 191
- Verbunt, F., & Hut, P. 1987, *The Origin and Evolution of Neutron Stars*, 125, 187
- Vesperini, E., & Heggie, D. C. 1997, *MNRAS*, 289, 898
- Vesperini, E., McMillan, S. L. W., D'Antona, F., & D'Ercole, A. 2013, *MNRAS*, 429, 1913
- Watkins, L. L., van der Marel, R. P., Bellini, A., & Anderson, J. 2015, *ApJ*, 803, 29